Labelled Object Velocimetry: Simultaneous Measurements of Bubble Size and Velocity

David Laupsien, Claude Le Men, Arnaud Cockx, Alain Line

Labelled Object Velocimetry: Simultaneous Measurements of Bubble Size and Velocity

David Laupsien[a,*], Claude Le Men[a,], Arnaud Cockx[a,], Alain Line[a,]

[a] *TBI, University of Toulouse, CNRS, INRA, INSA, Toulouse, France*

Abstract

This paper presents labelled-object velocimetry (LOV) - a technique to determine the velocities of labelled objects in multiphase flow. LOV is based on spatial correlations similar to those used in particle-image velocimetry (PIV) but employs grey-level shadowgraph images to determine object velocities. Object detection and labelling are performed using a classical image-processing algorithm. In contrast to PIV, interrogation areas in LOV are not uniformly distributed. Instead, these areas surround objects, and therefore, depend on object positions and sizes. Additionally, the proposed technique recalls a previously developed algorithm [1] to distinguish between single bubbles and complex situations, such as overlays, breakups and coalescences. This algorithm-based object selection (ABOS) provides a statistically reliable sample of the entire bubble swarm in terms of size and shape. Although both techniques are completely independent, they can be combined to link object velocities to their geometrical characteristics. Thus, the LOV technique can be used to ascertain velocity-object-diameter histograms.

Keywords: Object Labeling ; Sum of Absolute Differences (SAD) ; Bubble Dynamics ;

[*] Fully documented templates are available in the elsarticle package on CTAN.
[*] Corresponding author
Email address: `laupsien@insa-toulouse.fr` (David Laupsien)

1. Introduction

The information regarding bubble velocities associated with bubble size constitutes a crucial aspect of investigations, especially those concerning bubble columns widely used in chemical and biochemical industries. Bubble-induced hydrodynamics, which significantly influences the mass transfer and mixing abilities of multiphase flows, depends on bubble characteristics. However, acquisition of reliable experimental data requires precise measurements to be performed under practical operating conditions, wherein the bubble size may show large distribution. To this end, the use of non-intrusive techniques is being actively investigated, and several articles dedicated to their development can be found in literature. One of the simplest nonintrusive techniques involve following a demarcation line between the bubble and liquid zones upon completion of gas injection to estimate the overall swarm velocity [2]. Unfortunately, this method modifies the flow hydrodynamics drastically. Additionally, it is more applicable to steady flows with homogeneous spread in the bubble-column section. The past few decades have witnessed development of more sophisticated laser-based methods. In the 1970s, researchers [3] used laser Doppler anemometry (LDA), which is based on light scattering, or the Doppler Effect [4] to investigate bubble dynamics. More recently, an LDA-based technique was applied to rising microbubbles with dimensions up to 100 μm [5]. The LDA technique has also been extended to develop phase Doppler anemometry (PDA) based on refraction of light through one or more additional photo detectors. A major advantage of the PDA technique is its high data-acquisition rate, especially for turbulence statistical analysis. Nevertheless, applications of both LDA and PDA are limited to single-point measurements and spherical seeding particles. This implies that in cases involving gas-liquid flows in water without surfactants, use of these techniques is limited to bubble sizes (as tracer) of up to 1 mm [6]. Thus, in applications involving large, non-spherical, and deformable objects, particle tracking velocimetry (PTV) via high-speed CCD cameras is generally employed. Such optical methods facilitate investigation of two-phase flows in cross-sectional planes illuminated by a sheet of laser light or volumetric projection if backlighting is used. Several PTV techniques have been developed to perform bubble identification between two consecutive images by determining geometric similitudes [7]. In this case, velocity calculations can be performed based on either the geometric centre [8], centre of a projected ellipse [9]; [10], contour [11] or use of the front-tracking method also applicable to numerical data [12]. All tracking techniques are limited by comparable disadvantages. When using the front-tracking approach, errors may be incurred in cases involving large deformable bubbles or overlays of multiple bubbles rising at different velocities. Likewise, the geometric centre technique is limited to flows involving small bubbles owing to errors induced in the calculation of the geometric centre location caused by the viewing angle and bubble deformation. Another technique-bubble image velocimetry (BIV)-inspired by particle image velocimetry (PIV) has been proposed [13] [14]. BIV estimates velocity fields with uniformly distributed vectors using bubbles, or more precisely, the flow texture of a dense bubble swarm, instead of seeding particles, inside interrogation areas. In addition, it employs backlight instead of laser light for illumination. In a recent study [15], this method was applied to investigate bubble trajectories inside jet bubbling reactors. However, a major limitation of this method can be observed when analysing heterogeneous flows. If the interrogation area contains several bubbles with different velocities, the vector obtained represents the mean displacement or the centroid of the displacement probability density function rather than individual velocities of each object. In cases involving high field-of-view depth and large velocity variance between different flow planes, significant errors may be induced. In statistical approaches wherein object velocities are linked to their geometrical parameters, this problem can be addressed by performing algorithm-based object selection (ABOS). The labelled-object velocimetry (LOV) technique presented in this study is based on one such algorithm reported in an extant study [1]. The said algorithm uses bubble properties, such as size, eccentricity, and solidity. Another weakness of the BIV approach is that generation of large dark regions can be observed if the bubble size is very large compared to the interrogation area. It is well acknowledged that presence of an insufficient number of grey levels causes correlation functions to become noisy, which in turn, leads to attainment of inaccurate results. To the best of the authors' knowledge, the proposed method is the first of its kind to facilitate precise velocity measurements for all kinds of detected objects irrespective of their size or shape. The proposed digital image-processing technique can be adapted for the analysis of highly polydispersed flows. In addition, the proposed method can be combined with any algorithm capable of characterizing object geometries, such as machine-learning algorithm reported in [16] [17], thereby enabling simultaneous measurement of object size and geometry. Because the proposed technique does not involve particle tracking, no comparison of geometrical characteristics is required between frames. The velocity is directly calculated on the correlation function and no object identification is performed for the second frame. This has the advantage that the velocity-calculation remains unaffected if additional objects appear in the correlation field. One major advantage of this method is that underlying velocity calculations are based on the absolute difference function squared (ADF^2) approach developed by the observational astronomy community. ADF^2 is clearly superior to the Fast Fourier Transform (FFT)-based correlations concerning noise [18]. Thus, velocities of all particles - deformed, asymmetric, or distorted - can be estimated using the proposed approach owing to no comparison of their shapes between consecutive images. For example, the proposed LOV method was applied to a case involving bubbly flows with low void fractions ($< 1\%$) and heterogeneous distributions (in terms of both size and velocity). High-speed as well as classical PIV cameras in the double-frame mode can be used with backlight to enhance contrast between captured phases. Additionally, the proposed technique can be employed at any acquisition frequency provided the time interval between image pairs is short.

2. Data Treatment Development of Labeling, LOV & ABOS for simultaneous Velocity and Size Measurements

This section describes details concerning the data-processing strategy followed in this study. This strategy was divided into three independent parts. The first part involves performing basic image processing, wherein only the first frame of each image pair is treated and binarised for object detection and labelling. The second frame is subjected to a correlation-based blind research. The image-processing step serves for two purposes - (i) extracting interrogation-area positions and sizes for performing LOV and (ii) calculating values of geometrical parameters for ABOS. The second part of the data-processing strategy provides details regarding operating principles of the LOV technique. It includes the process for obtaining velocity vectors for each object type, thereby generating a shadow on the camera and independently of its nature. Plus, the precision realized via the use of the proposed technique is discussed. In the third part, the ABOS developed and reported in a previous study [1] is recalled. ABOS is capable of distinguishing between single or well-identified bubbles (WIBs) and so-called complex situations (CS). In the context of this study, instances of bubble overlay, coalescence and breakup are considered as complex situations. It is noteworthy that LOV and ABOS are independent of each other. However, combining both techniques (as described in section 3) can link object parameters, such as size and eccentricity, to corresponding object velocities. Thus, a large number of individual bubbles can be characterized as representative samples, and the swarm dynamics problem can be statistically analysed.

Image Treatment for Labeling. To label and distinguish each object that generates a continuous shadow (convex object), it is necessary to extract its position coordinates from the first frame of captured shadowgraph image pairs. To this, a classical image-processing technique was applied in this study. Per this technique, raw grey-level images (Fig. 1a) were transformed into binarised ones (Fig. 1d). Figure 1a depicts a magnified ($700 * 860$ px) view of a raw shadowgraph image of bubbly flow. Non-homogeneities due to LED background lighting were removed by capturing a flat image (i.e. an image of the acquisition-window background sans any bubbles). Each captured shadowgraph image was divided by the flat image. Consequently, the grey-level intensity of the resulting image was multiplied by the average value of the flat image. Subsequently, a grey-level filter was used to enhance the contrast further, thereby generating the final binarised image (Fig. 1b). The grey-level filter weights the relationship between input and output values to yield a darker output via application of the following equation instead of a linear function:

$$GL_{Out} = \frac{max(GL_{In}) * GL_{In}^{1/\sigma}}{max(GL_{Out})} \tag{1}$$

where GL denotes grey level. In this study, the value of σ was set as 2; however, this value can be increased further to weight darker pixels. The parameter $max(GL_{Out})$ depends on the colour depth of captured images and equals 256 for 8-bit images.

To determine the gas-liquid interface location, a grey-level-gradient threshold of 0.6 was applied. Pixels with grey levels below this value were considered corresponding to the gas phase, whereas those with higher grey levels were considered to correspond to liquids. Thus, as already stated, frame 1 of each image pair was binarised, as depicted in Fig. 1c, wherein black and white pixels correspond to liquid and gas phases, respectively. The last image-processing step comprised hole filling, wherein each white pixel was dilated isotropically by one pixel to close possible interface gaps. Subsequently, objects were filled with white pixels before being eroded isotropically by one pixel to attain their initial dimensions. The final binarised image of frame 1 (Fig. 1d) was then used for extracting labelled-object characteristics, such as position coordinates (those corresponding to the smallest possible rectangle surrounding the object) for LOV. In addition, solidity ratios were calculated, and ellipse projection was performed to obtain further information, such as eccentricity or orientation angle, for ABOS [1]. No labelling was performed on frame 2 of the captured image pairs, because object velocities were determined using correlation func-

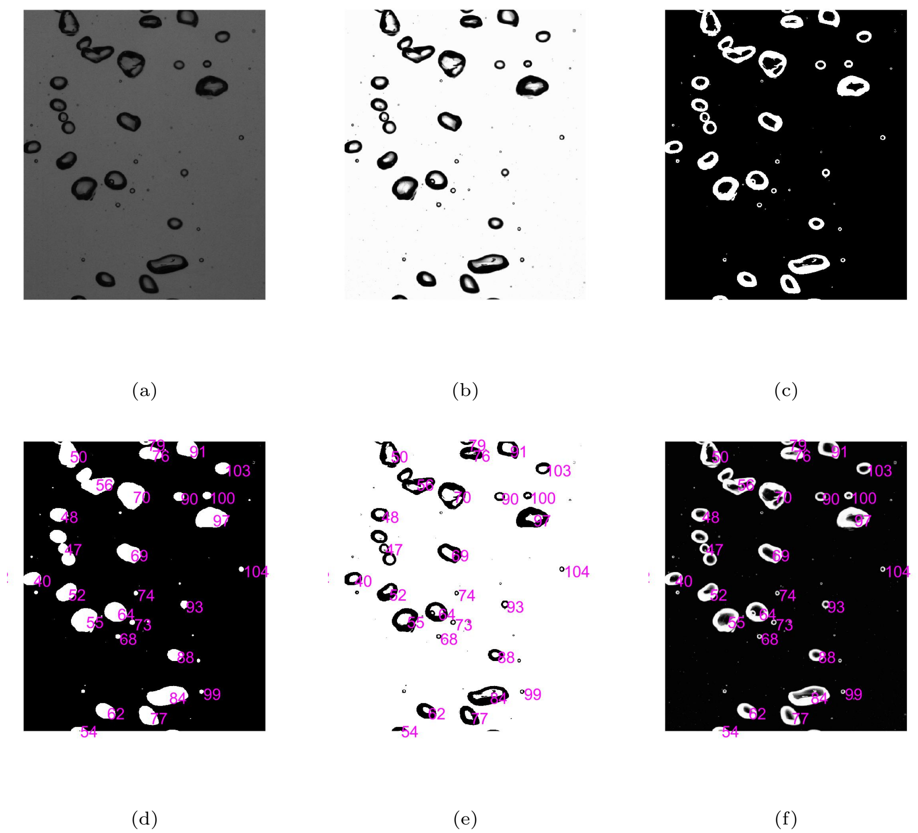

Figure 1: Water - Membrane Sparger - $100\frac{l}{h}$: Zoom on a) Raw Image b) Light Filtered Image c) Binarized Image d) Final Binarized Image e) Grey Level Image with Labeling f) Inverted Grey Level Image with Labeling

tions and not via geometrical similarity parameters. However, the said velocity calculations (section 2.2) require use of grey-level images. Therefore, all labels depicted in Fig. 1d were projected onto frame 1 from Fig. 1b, thereby providing a grey-level image with required labelling (Fig. 1e). As a final step, black and white gradients on grey-level images must be inverted to obtain Fig. 1f, thereby saving computational time in cases where the camera captures more liquid than gas.

Velocity Calculation on Grey Level Images. Double-frame acquisition performed in LOV is similar to that in PIV. Likewise, the application of spatial correlation to image pairs separated by short time intervals is also similar in both techniques. The main difference between LOV and PIV concerns interrogation areas, the assigning of a velocity vector to each of them, and corresponding correlation functions. PIV or BIV [13] images are usually divided into uniformly distributed interrogation areas based on seeding-particle density, whereas the number and size of interrogation areas in LOV images depend directly on the number and size of labelled objects. In this regard, the LOV technique can be considered equivalent to a Lagrangian approach with interrogation areas surrounding each object.

As aforementioned, coordinates of the smallest possible rectangles surrounding each labelled object were extracted from frame 1 of binarised image pairs and projected onto frame 1 of inverted grey-level ones, as described in Fig. 2 (left). Notably, spatial correlations must be applied exclusively to raw or grey-level images and not binarised ones. Grey-level gradients observed at bubble interfaces facilitate seamless inter-correlation. The observed large spread of grey levels makes the correlation more efficient compared to PIV images, wherein most pixels are dark. However, correlation fields in LOV are obtained by scanning (extending) interrogation areas comprising a large yet identical number pixels in all directions around the initial object position (centre of the rectangle around an object). Thus, the scan size represents a compromise. This is because on one hand, the scan must be sufficiently large to capture the object in the second frame, and hence, it must be defined by the maximum object velocity in the dispersed phase. On the other hand, the scan must be small enough to prevent appearance of other objects within the correlation field. In this way, potential object mix-ups, and consequently, erroneous velocity-vector calculations can be avoided. In the present study, a scan length of 11 px along each direction was considered sufficient to obtain valid velocity vectors. In accordance with the scale (0.1 mm with $\Delta t = 2ms$) used in this study, an 11-pixel scan length represents a maximum velocity of $0.55m/s$. Nevertheless, a safety measure was included in the correlation process. For displacement equal to or exceeding 10 px, the interrogation area was moved by the same number of pixels along a velocity-vector component before performing a second spatial correlation. In this case, the final vector would correspond to the resultant of the first and second vectors.

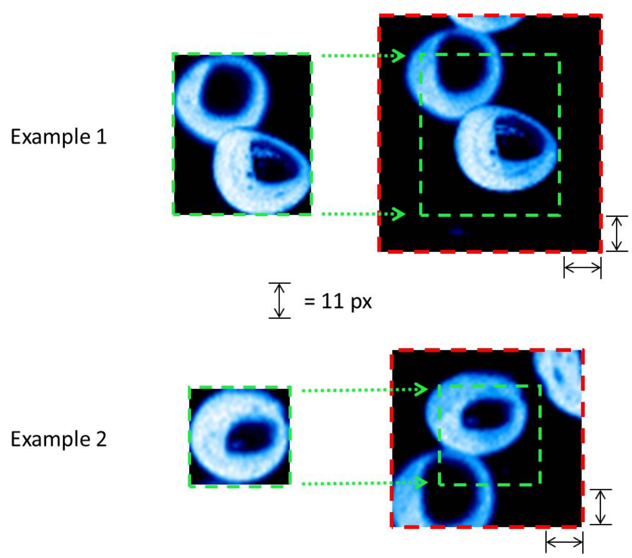

Figure 2: 2 Examples of Double Frame Image Pairs - Left: Frame 1 with the smallest possible Rectangle surrounding the Object ; Right: Frame 2 with the Projection of the Rectangle from Frame 1 + Scan of 11 *pixels*

The velocity-calculation process can be divided into two parts. The first part involves use of a spatial correlation. In this study, the absolute difference function squared (ADF^2) approach based on the sum of absolute differences (SAD) was preferred owing to its adequate accuracy and fast calculation [18]. The correlation function can be expressed as:

$$ADF^2 = \left(\sum_{x,y} |g(x,y) - g_{ref}(x+i, y+j)| \right)^2 \quad (2)$$

where g denotes the interrogation area in frame 1; g_{ref} denotes correlation field in frame 2; x & y denote the horizontal and vertical grid positions, respectively; and i & j denote the horizontal and vertical pixel shifts, respectively. The interrogation area g from frame 1 is moved one pixel at a time inside g_{ref} in frame 2 ($(i,j) \in [-scan, scan]$). At every position equation 2 was applied to all pixels within g and g_{ref} for all pixel shift values i and j to obtain the final correlation function for each individual pixel. The said final function has constant size of $23 * 23\ px$ $((2 * scan + 1) * (2 * scan + 1))$. This constitutes the main difference between the LOV and PIV approaches. Whereas FFT-based correlations are applied to fixed interrogation areas in PIV, ADF^2 correlations applied to larger interrogation areas are used in LOV to minimize noise, as reported in [18]. The authors investigated the intensity mismatch (bias), image noise, shift, and root mean square (RMS) errors for five correlation methods and four interpolation algorithms applied to synthetic images with known shifts and noise levels. Based on the findings from this investigation, the authors recommended using square difference function (SDF) or ADF^2 approaches to calculate correlation functions. The precision of the displacement calculated in this first step of velocity calculation was 1 px.

The second part of the velocity calculation process comprises subpixel interpolation around the global maximum of the correlation function (ADF^2). In this way, the accuracy of velocity-vector calculations can be improved to subpixel levels. Author et al. [18] recommend use of the 2D least squares or 2D quadratic interpolation methods. Accordingly, the biparabolic fit corresponding to 2D quadratic interpolation was considered in this study. The said fit yields the best results when applied to $3 * 3$-elements of the correlation function, as suggested in [19], wherein the authors explain how use of lower- and higher-order polynomials tend to over- and underestimate the shift, respectively. In addition, it must be remembered that correlation functions might not necessarily be symmetric, and one must determine the position of the maximum (and not median) value of the correlation function. This is another reason for considering $3 * 3$-elements around the maximum value of the correlation function. Correlation functions corresponding to objects depicted in Fig. 2 are presented in Fig. 3. As can be observed, in the first example, the labelled object considered does not change between frames. Hence, the obtained correlation function only shows a global maximum (Fig. 3), and therefore, the object velocity can be easily determined. In the second example considering the object in frame 2 from Fig. 2 (left), another object of similar size can be observed to lie almost entirely within the correlation field. Accordingly, the corresponding correlation function (Fig. 3) is characterised by two maxima—global and local. This example helps one appreciate the superiority of the use of LOV technique compared to tracking methods that require both image frames captured to be geometrically similar. When using LOV, the appearance of additional bubbles in the correlation field causes additional peaks to appear in the correlation function. However, the velocity-calculation remains unaffected because the correlation function obtained is characterized by a clear global maximum corresponding to the labelled object obtained from frame 1. Thus, objects in frame 2 need not be identified as overlays of multiple bubbles, and no object separation needs to be performed. It is noteworthy to mention that the greater the similarity between objects the higher is the resulting correlation function. Therefore, the time interval considered ($\Delta t = 2ms$, as considered in this study) must be short enough to avoid distortions. The final displacement between the centre of the interrogation area and correlation maximum is indicated by an arrow, as depicted in Fig. 3. Thus, knowing the time interval between captured frames, an object's velocity can be easily deduced.

The proposed method can be applied to all connected objects in an image pair, thereby yielding a velocity map similar to that shown in Fig. 4. Inde-

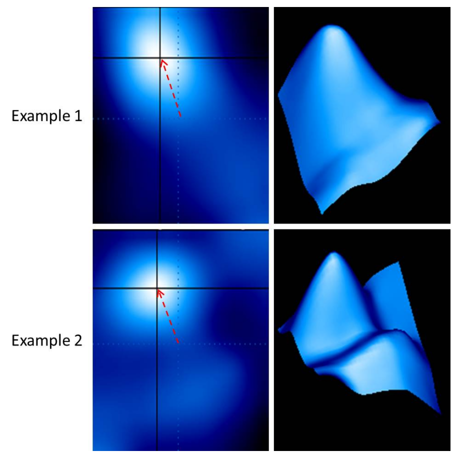

Figure 3: Left: 2D Correlation Function ; Right: 3D Correlation Surface (all Scans show a Size of $23 * 23$ pixels)

pendent of its nature—single, coalescing, breaking, or overlapping—each object (bubble) detected and labelled in frame 1 of a captured image pair can be represented by an arrow indicating the direction and magnitude of its velocity.

The uncertainty of velocity measurement depends on the estimation of the subpixel position of the correlation function's maximum. As reported in [19], subpixel precision corresponds to the inverse of scan width. In this study, this width equalled 23 px (11 px along all directions around the labelled object), thereby yielding a shift accuracy of $\frac{1}{23}$ times a pixel. It is important to note here (as well as when using PIV) that velocity uncertainty is absolute irrespective of the magnitude of the velocity vector. In the present case, one pixel corresponds to 0.1 mm, and given the time interval of 2 ms between capturing of successive image pairs, a shift accuracy of $\frac{1}{23}$ times a pixel yields an absolute uncertainty of 0.22 mm/s. Thus, the precision as well as the entire velocity-calculation process is independent of object size and shape. In addition, it must be realized that when the correlation function becomes too wide, another limitation on its accuracy appears owing to flatness around the observed maximum. However, the correlation function usually maintains a good height-to-width (aspect) ratio

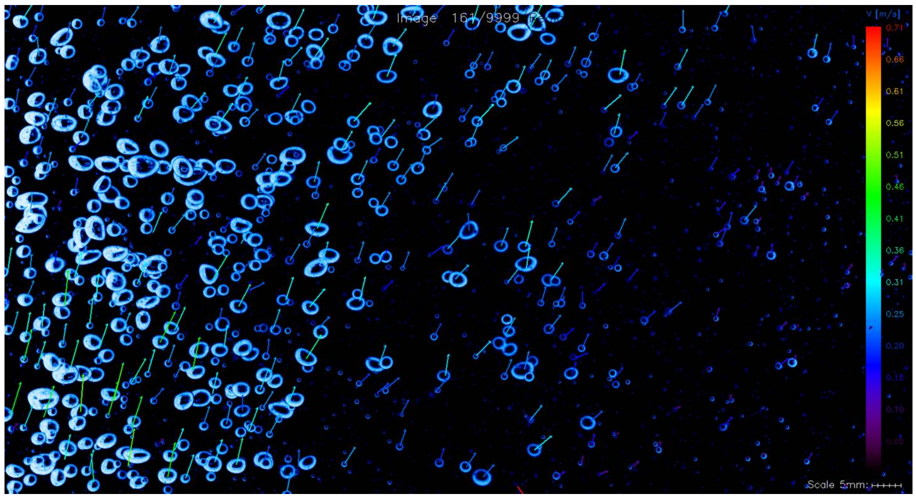

Figure 4: Example of a Velocity Field obtained via LOV without object selection (without ABOS)

because ADF^2 performs a summation of grey levels of all pixels inside the interrogation area (equation 2). This property is further enhanced by the large spread of grey levels induced by the gas-liquid interface. Assuming a $5 * 5$ mm ($50 * 50$ px) interrogation area, each point on the ADF^2 correlation function is the result of $50 * 50$ times the absolute difference and $50 * 50$ times the sum, corresponding to $N_{sum} = (50 * 50)^2$. Considering camera-induced noise being random, correlation function's noise can be subsequently reduced by a factor of $\sqrt{N_{sum}} = 50 * 50$. Thus, the correlation function becomes extremely smooth by a factor equal to the number of pixels in the initial interrogation area. Hence, the height of the correlation function corresponding to a 5-mm ellipsoidal bubble (refer example 2 in Fig. 2) significantly exceeds its width, as shown in Fig. 3. Moreover, none of the objects considered in this study were even close to being large enough (up to 40 mm) to match this upper limit of the correlation function induced by the maximum's flatness.

Bubble Identification on Binarized Images. As already mentioned in preceding sections, a velocity vector corresponding to each labelled object in frame 1 of an image pair was obtained in this study independent of the object's nature. This section describes how ABOS can be performed to separate single or well-identified bubbles (WIBs) from complex situations (CS) involving overlaying, coalescing, and/or breaking bubbles. Thus, it is possible to consider data only from individual bubbles to link their characteristics to corresponding velocity vectors for statistical analysis. To this end, object parameters, such as their size (defined as diameter DE of an equivalent sphere), eccentricity, orientation (angle between the horizontal and major axis of a projected ellipse), and solidity were used. Values of these parameters can be extracted from corresponding binarised images (Fig. 1d) after performing ellipse projection for each labelled object. ABOS aims to obtain a statistically reliable sample representative of the entire bubble swarm. The filter strategy presented in Fig. 5 was used for this purpose. The first step in this regard involved ensuring the object is not intersected by image borders. Subsequently, solidity was considered as the first filtering parameter, the threshold value of which varies with object size—from 0.97 (for small bubbles) to 0.9 (for large bubbles). Likewise, eccentricity was considered the second filtering parameter for objects with equivalent diameters measuring less than 7.5 mm. For larger objects, their orientation was considered the second filter. In this manner, all objects were categorized as either WIB (ellipsoidal bubbles and spherical caps) or CS. For further details, readers may please refer [1]. With the certainty to consider objects as WIBs exclusively, one linked object velocities to their geometric parameter, in particular, their size. Thus, by combining the techniques presented in sections 2.2 and 2.3 with a large number of WIBs, statistical data analyses of complete bubble-flow dynamic could be performed.

3. Examples of Application

Two bubbly-flow scenarios were considered in this study to demonstrate the performance of the proposed LOV technique. Both cases were investigated in a pseudo two-dimensional bubble column described in section 3.1. The first case

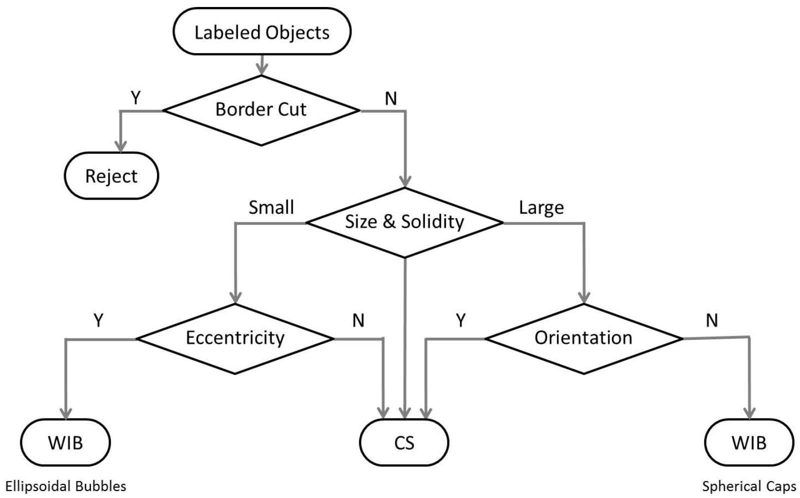

Figure 5: ABOS Filter Strategy for Bubble Identification out of Labeled Objects ; Y = Yes ; N = No ; WIB = Well Identified Bubble ; CS = Complex Situation

involves an oscillating bubble plume with ellipsoidal 100 l/h bubble injection in water using a membrane sparger. The oscillating plume can also be categorized as vortical flow [20], and it is characterised by a heterogeneous velocity distribution. A shadowgraph image of the acquisition window captured under said flow conditions is depicted in Fig. 6a. The second example corresponds to a bubble jet with spherical-cap injection at 50 l/h in liquid B5 (with 100 times the viscosity of water) using a slugflow sparger. Bubbles were observed to rise along the centre of the column. The said bubbles remained isolated and did not form a bubble swarm (refer Fig. 6b). The observed flow structure can be considered to correspond to double-cell transition flow [20], and no low-frequency oscillations were observed. This case was considered owing to its bimodal size distribution.

Experimental Setup. As stated above, experiments in this study were performed using a pseudo two-dimensional bubble column measuring 0.06 m deep, 0.35 m wide and 2 m high, thereby allowing the capture of shadowgraph images. Details regarding the experimental setup and measurement method are presented

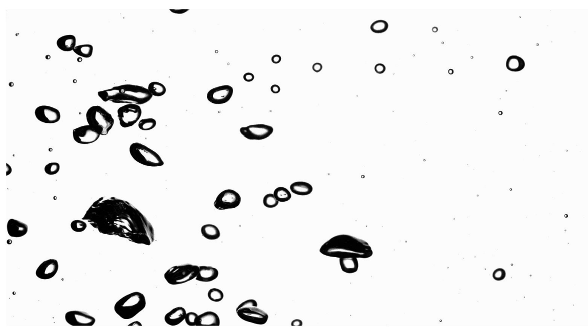

(a)

(b)

Figure 6: Examples of Applications: a) Water - Membrane Sparger - $100\frac{l}{h}$; Vortical Flow b) Breox (24%) - Slugflow Sparger - $50\frac{l}{h}$; Double Cell Transition Flow

in a previous study [1]. Figure 7 depicts a sketch of the experimental setup, which clearly shows the acquisition window. The X-axis represents the horizontal component. The width dimension was normalised with respect to half the column width, thereby causing column-wall positions to correspond to values of -1 and 1 on the horizontal axis with the column centreline located at zero. Bubble injection was performed using two different spargers located at the centre of the column bottom. Ellipsoidal bubbles or spherical caps were injected into the bubble column using a membrane or slugflow sparger, respectively [1]. Water (example 1) and Breox (example 2)-a Newtonian fluid with viscosity 100 times that of water-were considered in this study. The properties of Breox are listed in Table 1.

Images were captured using the Dantec 2M camera in the double-frame (PIV) mode. The image resolution was set to $1600 * 840$ px, which corresponds to $167 * 87$ mm^2 image area. As observed in Fig. 7, the acquisition window was located at the centre of the liquid column measuring 1.3 m, and it nearly covers the entire right half of the column width. To facilitate data analysis, the acquisition-window width was discretized into 70 spatial intervals of 23 px each. In both cases, the analysis was restricted to objects located inside two intervals around a certain point ($X = 0.25$ or $X = 0.07$). Thus, the area of interest measured 46 px or 4.7-mm wide. The field of view accounted for the entire column depth (60 mm). The acquisition frequency and time interval between captured image pairs were set to 15 Hz and 2 ms, respectively. Because of low-frequency bubble-plume oscillations of period 22 s, measurements were required to be performed over an 11-min duration to capture a sufficient large number of periods (30 periods corresponding to $10,000$ image pairs). In this manner, statistically reliable data were obtained for both experiments, despite performing the initial WIB discrimination.

Example 1: Oscillating Bubble Plume. The first practical example considered in this study involved an ellipsoidal bubble plume oscillating with a period of 22 s [21]. The plume was observed to move from one side of the liquid column

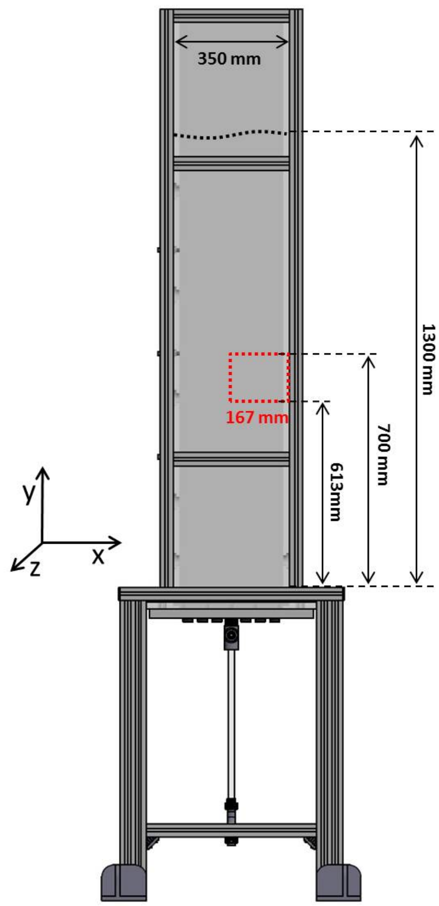

Figure 7: Experimental Setup

Fluid	Ref.	Surface Tension (mN/m)	Viscosity (mPa.s)
Water	W	75.1	1
Breox (24%)	B	55.0	100

Table 1: Fluid Properties

to another, thereby covering almost the entire column section whilst generating bimodal velocity distributions. Under the experimental conditions considered in this study, a low rate of coalescence was observed, and the mean bubble diameter (D_E) equalled 5.6 mm [1]. From the 10,000 image pairs captured in this experiment, 134,229 and 53,578 objects were identified as WIBs and CS, respectively, thereby corresponding to a WIB concentration of 71.5%. Thus, the WIB sample was considered statistically representative of the entire bubble swarm. The following analysis focuses on objects captured in two spatial intervals around $X = 0.25$ (corresponding to a distance of 44 mm from the column centre). This above value of X was considered because it corresponds to the location of the maximum value of the horizontal time-averaged void-fraction profile [22].

Moreover, the proposed LOV technique assigned a velocity vector linked to the equivalent diameter of each object. Use of the LOV technique facilitated the generation of two-dimensional histograms depicted in Fig. 8. Figures 8a and 8c depict observed trends in the vertical and horizontal velocity components, respectively, with respect to equivalent diameters of identified WIBs. As can be confirmed, the vertical velocity component demonstrates a peak at $U_{vertical} \approx 0.35 m/s$ and $D_E \approx 5mm$. This velocity represents the summation of the free velocity ($U_{vertical} \approx 0.25m/s$) of an ellipsoid bubble rising in a quiescent liquid and mean liquid velocity ($U_{L_{MEAN}} \approx 0.05m/s$ [22]) of the bubble plume. The large velocity distribution observed can be explained based on the oscillating-plume behaviour. Under the experimental conditions considered in this study, liquid-velocity fluctuations at point $X = 0.25$ (of the order of $U_{L_{RMS}} \approx 0.15m/s$ [22]) influence the rising velocity of bubbles, thereby resulting in a large velocity spread. Along the horizontal direction, Fig. 8c reveals the presence of a nearly symmetric bimodal velocity distribution created by the lateral bubble-plume movement inside the liquid column. Figures 8(b) and 8(d) demonstrate similar trends for CS objects. As can be observed in Figs. 8b and 8d, fewer CS objects were identified compared to WIBs. Moreover, the observed range of CS-object size also exceeds that of corresponding with WIBs. In accordance with the hydrodynamic structure of objects considered in this case, similar velocity ranges were observed for both CS objects and WIBs. Additionally, in this case, CS objects demonstrated only overlays with no instances of coalescence or breakup. These overlays comprised multiple bubbles in different planes moving at nearly identical velocities, which were also similar to those of WIBs.

This trend can be confirmed with reference to Fig. 9 that depicts size-independent velocity histograms plotted along both directions. Distributions of both WIBs and CS objects were normalized based on their number, and both distributions are depicted in the figure. As expected, in view of the aforementioned results, both WIBs and CS objects demonstrate similar velocity trends. As observed, the vertical-velocity distribution demonstrates the same rising velocity $U_{vertical} \approx 0.35m/s$, whereas the horizontal component demonstrates a bimodal shape with two clear peaks. The slightly higher peak observed in the positive range in Fig. 9b is caused by decentralization of the measurement position towards the right. At this point, bubbles tend to move slightly further away from the centre.

Clear differences between WIB and CS-object size distributions can be observed. Figure 10 depicts equivalent-diameter histograms for WIBs and CS objects normalized based on their total count. In the case of WIBs, a large peak can be observed close to 5 mm, whereas for CS objects, the corresponding peak appears around 7.5 mm. Once again, because no coalescence was observed in this case, bubble overlays lead to formation of large objects. The observed size difference illustrates the importance of bubble selection to avoid overestimations.

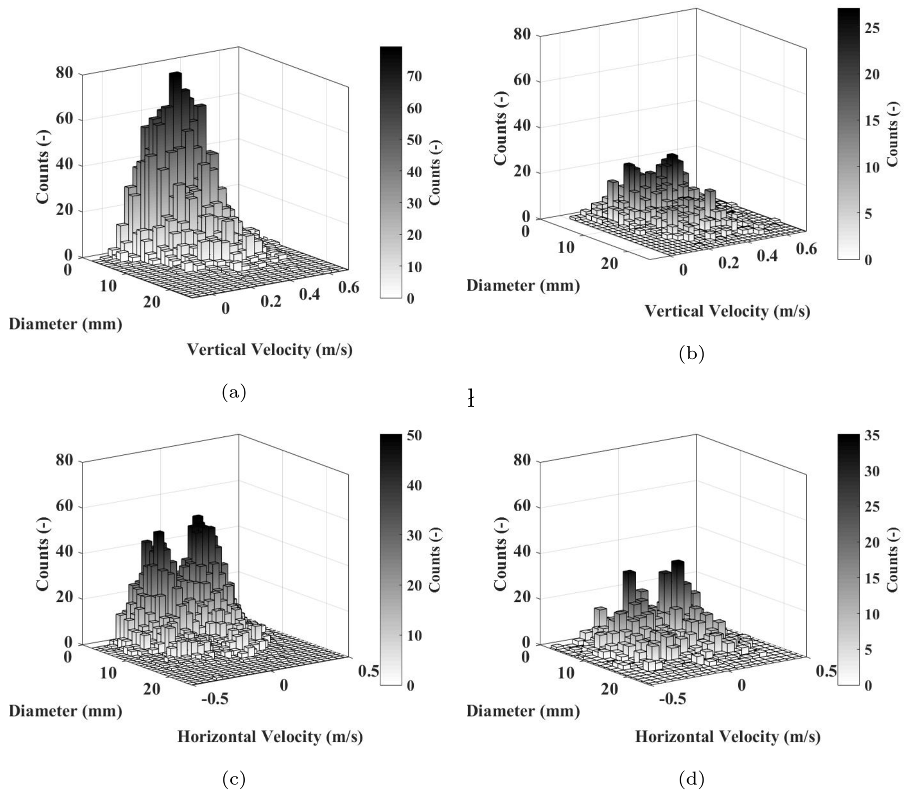

Figure 8: Water - Membrane Sparger - $100\frac{l}{h}$: Velocity-Diameter Histograms from measurments in point $X = 0.25$ for the Vertical Component in the case of a) WIB and b) CS ; and the Horizontal Component and in the case of c) WIB and d) CS

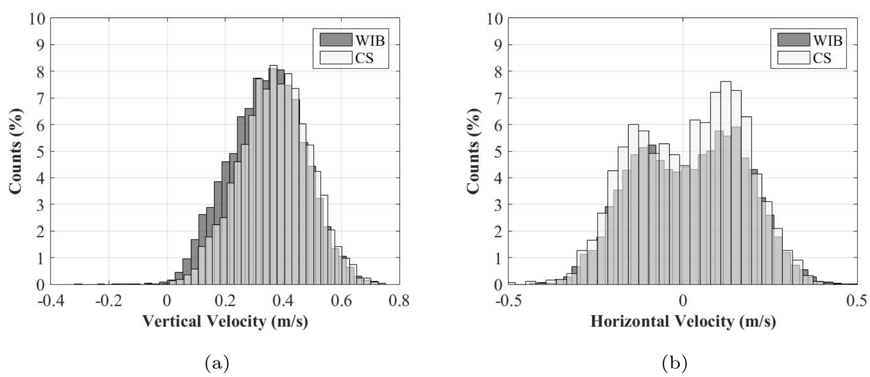

Figure 9: Water - Membrane Sparger - $100\frac{l}{h}$: Velocity Distributions in Point $X = 0.25$ a) Vertical and b) Horizontal Component

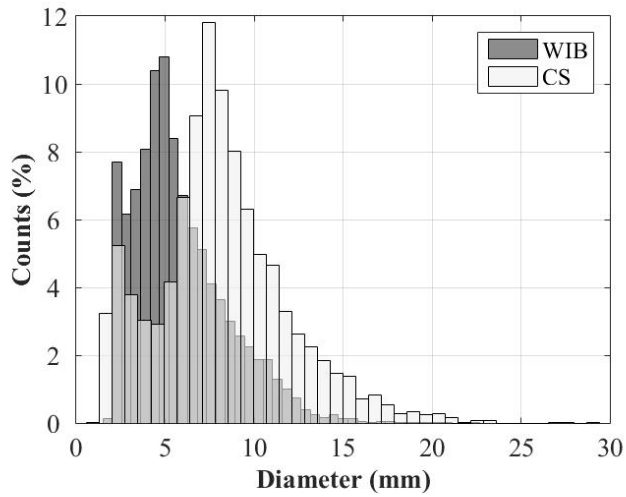

Figure 10: Water - Membrane Sparger - $100\frac{l}{h}$: Bubble Size Distributions in Point $X = 0.25$

Example 2: Double Cell Transition Flow. To demonstrate the effectiveness of the proposed LOV method further, its application to a second practical case involving WIBs exclusively (for the sake of simplicity) is presented herein. In this case, large bubbles were injected into a highly viscous fluid (Fluid B) using a slugflow sparger, thereby resulting in a non-oscillating "Double-cell Transition Flow" (DCTF) [20]. Because horizontal-velocity fluctuations assume less importance in this case, the analysis mainly focussed on the vertical-velocity component. This case was primarily selected in view of its bimodal bubble-size distribution. Bubbles may have aspired into the wake of a large one rising in front of it, thereby resulting in their coalescence, which in turn, creates large spherical caps (Fig. 6b) along with a large size spread. In this case, $8,703$ WIBs were identified out of $13,414$ objects, thereby corresponding to 65% WIB concentration. Bubbles were observed to rise along the centre of the liquid column, similar to a bubble train. Hence, the maximum value of the time-averaged horizontal void-fraction profile was observed to be located along the column centre. Accordingly, the point located at $X = 0.07$ [22] was considered for data analysis.

Figure 11 depicts a two-dimensional histogram of the vertical velocity com-

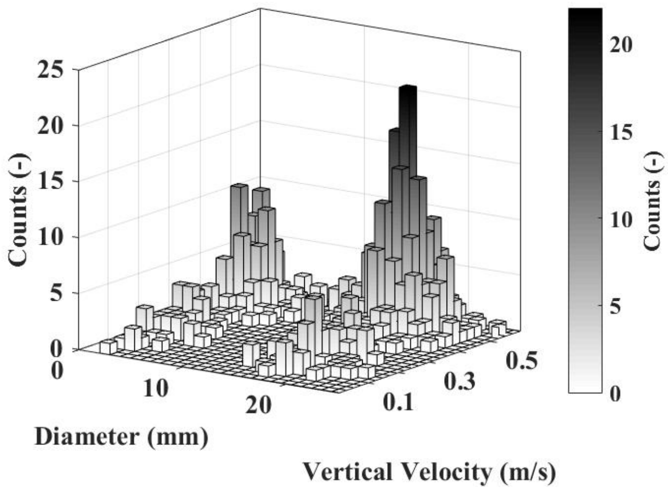

Figure 11: Liquid B - Slugflow Sparger - $50\frac{l}{h}$: Velocity Size Distributions in point $X = 0.07$ in Vertical Component

ponent with respect to the equivalent WIB diameter, and occurrence of two clear peaks—around 2 mm and around 15 mm-can be observed. These observed peaks correspond to a similar velocity value $U_{vertical} \approx 0.45 m/s$. This result can be confirmed with reference to Fig. 12a, wherein the global peak corresponds to the same velocity. This velocity value can be explained based on the flow structure that results in generation of the mean liquid velocity $U_{L_{MEAN}} \approx 0.2 m/s$ [22]. By adding the value of the free vertical velocity ($U_{vertical} \approx 0.25 m/s$) of rising spherical caps in a quiescent liquid to $U_{L_{MEAN}}$, the resulting value of $U_{vertical} \approx 0.45 m/s$ can be obtained. It is noteworthy that bubbles of all considered sizes (ellipsoidal and caps) attain such high velocities (refer Fig. 12). Figure 12b illustrates the large range of bubble sizes. As can be confirmed, the first peak corresponds to ellipsoidal bubbles, whereas the second peak represents large spherical caps.

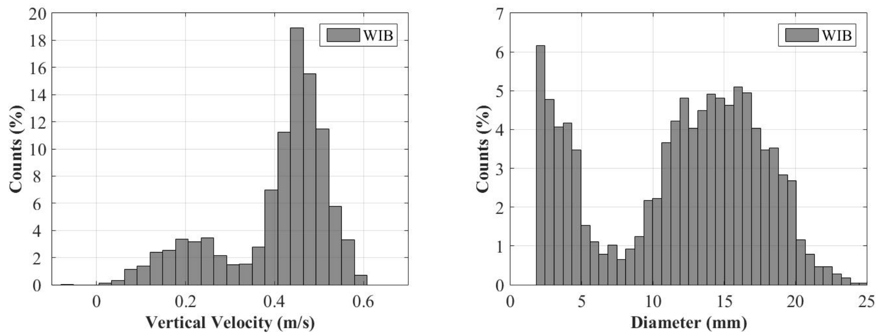

(a) (b)

Figure 12: Liquid B - Slugflow Sparger - $50\frac{l}{h}$: a) Velocity Distributions (Vertical Component) and b) Size Distribution in point $X = 0.07$

4. Conclusion

This paper presents a Lagrangian approach, referred to as the "labelled-object velocimetry (LOV)" technique, to assign individual velocity vectors to labelled objects identified in multiphase fluid-flow scenarios. The proposed LOV technique is based on the processing of grey-level shadowgraph images with subpixel precision. The underlying intercorrelation technique has been extensively discussed, and its realizable level of precision has been adequately demonstrated. In addition, application of an independent image-analysis method, called "algorithm-based object selection (ABOS)" has also been explained. It has been demonstrated how combining both above-mentioned approaches facilitates simultaneous measurement of bubble characteristics and individual object velocities. In this way, the proposed study establishes a link between sizes and velocities of statistically representative samples of entire bubble swarms. The effectiveness of the proposed method has been illustrated via consideration of its application in two practical scenarios involving flow of ellipsoidal bubbles and spherical caps.

References

References

[1] D. Laupsien, C. Le Men, A. Cockx, A. Liné, Image processing for bubble morphology characteristics in diluted bubble swarms, Physics of Fluids 31 (5) (2019) 053306. doi:10.1063/1.5088945.
URL https://aip.scitation.org/doi/10.1063/1.5088945

[2] D. J. Nicklin, Two-phase bubble flow, Chemical Engineering Science 17 (9) (1962) 693–702. doi:10.1016/0009-2509(62)85027-1.
URL http://www.sciencedirect.com/science/article/pii/0009250962850271

[3] R. Mahalingam, R. S. Limaye, J. A. Brink, Velocity measurements in two-phase bubble-flow regime with laser-doppler anemometry, AIChE Journal 22 (6) (1976) 1152–1155. doi:10.1002/aic.690220631.
URL https://aiche.onlinelibrary.wiley.com/doi/abs/10.1002/aic.690220631

[4] C. P. Wang, A unified analysis on laser Doppler velocimeters, Journal of Physics E: Scientific Instruments 5 (8) (1972) 763–766. doi:10.1088/0022-3735/5/8/016.

[5] G. H. Kelsall, S. Tang, A. L. Smith, S. Yurdakul, Measurement of rise and electrophoretic velocities of gas bubbles, Journal of the Chemical Society, Faraday Transactions 92 (20) (1996) 3879–3885. doi:10.1039/FT9969203879.
URL https://pubs.rsc.org/en/content/articlelanding/1996/ft/ft9969203879

[6] Z. W. Gan, S. C. M. Yu, A. W. K. Law, Hydrodynamic stability of a bubble column with a bottom-mounted point air source, Chemical Engineering Science 66 (21) (2011) 5338–5356. doi:10.1016/j.ces.2011.07.032.

URL http://www.sciencedirect.com/science/article/pii/S0009250911004945

[7] C. A. Acuna, J. A. Finch, Tracking velocity of multiple bubbles in a swarm, International Journal of Mineral Processing 94 (3-4) (2010) 147–158. doi:10.1016/j.minpro.2010.02.001.

[8] D. Colombet, D. Legendre, A. Cockx, P. Guiraud, F. Risso, C. Daniel, S. Galinat, Experimental study of mass transfer in a dense bubble swarm, Chemical Engineering Science 66 (14) (2011) 3432–3440. doi:10.1016/j.ces.2011.01.020.
URL http://www.sciencedirect.com/science/article/pii/S0009250911000303

[9] K. Ellingsen, F. Risso, On the rise of an ellipsoidal bubble in water: oscillatory paths and liquid-induced velocity, Journal of Fluid Mechanics 440 (2001) 235–268. doi:10.1017/S0022112001004761.
URL https://www.cambridge.org/core/journals/journal-of-fluid-mechanics/article/on-the-rise-of-an-ellipsoidal-bubble-in-water-oscillatory-paths-and-liquidinduced-velo
C4D609D39DD664C8FE5903AD66805B63

[10] M. Maldonado, J. J. Quinn, C. O. Gomez, J. A. Finch, An experimental study examining the relationship between bubble shape and rise velocity, Chemical Engineering Science 98 (2013) 7–11. doi:10.1016/j.ces.2013.04.050.
URL http://www.sciencedirect.com/science/article/pii/S0009250913003187

[11] R. F. L. Cerqueira, E. E. Paladino, B. K. Ynumaru, C. R. Maliska, Image processing techniques for the measurement of two-phase bubbly pipe flows using particle image and tracking velocimetry (PIV/PTV), Chemical Engineering Science 189 (2018) 1–23. doi:10.1016/j.ces.2018.05.029.

URL http://www.sciencedirect.com/science/article/pii/S0009250918303269

[12] J. Xue, M. Al-Dahhan, M. P. Dudukovic, R. F. Mudde, Bubble velocity, size, and interfacial area measurements in a bubble column by four-point optical probe, AIChE Journal 54 (2) (2008) 350–363. doi:10.1002/aic.11386.
URL http://onlinelibrary.wiley.com/doi/10.1002/aic.11386/abstract

[13] Y. Ryu, K.-A. Chang, H.-J. Lim, Use of bubble image velocimetry for measurement of plunging wave impinging on structure and associated greenwater, Measurement Science and Technology 16 (10) (2005) 1945–1953. doi:10.1088/0957-0233/16/10/009.

[14] D. Broder, M. Sommerfeld, Combined PIV/PTV-Measurements for the Analysis of Bubble Interactions and Coalescence in a Turbulent Flow, The Canadian Journal of Chemical Engineering 81 (3-4) (2003) 756–763. doi:10.1002/cjce.5450810356.
URL https://onlinelibrary.wiley.com/doi/abs/10.1002/cjce.5450810356

[15] Y. Shuai, X. Guo, H. Wang, Z. Huang, Y. Yang, J. Sun, J. Wang, Y. Yang, Characterization of the bubble swarm trajectory in a jet bubbling reactor, AIChE Journal 65 (5) (2019) e16565. doi:10.1002/aic.16565.
URL https://aiche.onlinelibrary.wiley.com/doi/abs/10.1002/aic.16565

[16] T. Haas, C. Schubert, M. Eickhoff, H. Pfeifer, BubCNN: Bubble detection using Faster RCNN and shape regression network, Chemical Engineering Science 216 (2020) 115467. doi:10.1016/j.ces.2019.115467.
URL http://www.sciencedirect.com/science/article/pii/S0009250919309571

[17] I. Poletaev, M. P. Tokarev, K. S. Pervunin, Bubble patterns recognition using neural networks: Application to the analysis of a two-phase bubbly jet, International Journal of Multiphase Flow 126 (2020) 103194. doi:10.1016/j.ijmultiphaseflow.2019.103194.
URL http://www.sciencedirect.com/science/article/pii/S0301932219305701

[18] M. G. Lofdahl, Evaluation of image-shift measurement algorithms for solar Shack-Hartmann wavefront sensors, Astronomy & Astrophysics 524 (2010) A90. doi:10.1051/0004-6361/201015331.
URL http://arxiv.org/abs/1009.3401

[19] L. J. November, G. W. Simon, Precise proper-motion measurement of solar granulation, The Astrophysical Journal 333 (1988) 427–442. doi:10.1086/166758.
URL http://adsabs.harvard.edu/abs/1988ApJ...333..427N

[20] M. E. Diaz, F. J. Montes, M. A. Galán, Influence of Aspect Ratio and Superficial Gas Velocity on the Evolution of Unsteady Flow Structures and Flow Transitions in a Rectangular Two-Dimensional Bubble Column, Industrial & Engineering Chemistry Research 45 (21) (2006) 7301–7312. doi:10.1021/ie060466b.
URL http://dx.doi.org/10.1021/ie060466b

[21] D. Laupsien, A. Cockx, A. Line, Bubble Plume Oscillations in Viscous Fluids, Chemical Engineering & Technology 40 (8) (2017) 1484–1493. doi:10.1002/ceat.201600690.
URL https://onlinelibrary.wiley.com/doi/abs/10.1002/ceat.201600690

[22] D. Laupsien, Hydrodynamics, Mass Transfer and Mixing induced by Bubble Plumes in Viscous Fluids, thesis, Toulouse, INSA (Dec. 2017).
URL http://www.theses.fr/2017ISAT0023